Ferroic clustering and phonon anomalies in Pb-based perovskite-type relaxors

2007 J. Phys.: Condens. Matter 19 275205

(http://iopscience.iop.org/0953-8984/19/27/275205)

IOP PUBLISHING JOURNAL OF PHYSICS: CONDENSED MATTER

J. Phys.: Condens. Matter **19** (2007) 275205 (10pp) doi:10.1088/0953-8984/19/27/275205

Ferroic clustering and phonon anomalies in Pb-based perovskite-type relaxors

B Mihailova[1,4], M Gospodinov[2], B Güttler[3], R Stosch[3] and U Bismayer[1]

[1] Mineralogisch-Petrographisches Institut, Universität Hamburg, Grindelallee 48, D-20146 Hamburg, Germany
[2] Institute of Solid State Physics, Bulgarian Academy of Sciences, Boulevard Tzarigradsko Chausse 72, 1784 Sofia, Bulgaria
[3] Physikalisch-Technische Bundesanstalt, Bundesallee 100, 38116 Braunschweig, Germany

E-mail: mi0a007@uni-hamburg.de

Received 16 December 2006, in final form 1 February 2007
Published 1 June 2007
Online at stacks.iop.org/JPhysCM/19/275205

Abstract

The phonon anomalies and their relationship to the structural inhomogeneities in Pb-based relaxors are studied on the basis of stoichiometric $PbSc_{0.5}Ta_{0.5}O_3$ and $PbSc_{0.5}Nb_{0.5}O_3$ and Nb-, Sn- and Ba-containing $PbSc_{0.5}Ta_{0.5}O_3$. The ferroic clustering and the development of the ferroelectric state can be followed by analysing quantitatively the intensity ratios of the Raman scattering arising from the corresponding local structural distortions. $PbSc_{0.5}Ta_{0.5}O_3$ and $PbSc_{0.5}Nb_{0.5}O_3$ differ from each other in the length of coherence of Pb shifts from the O layers, which leads to dissimilarities in the ferroelectric state. The incorporation of additional elements in the cation positions heavily influences the incipient ferroic species and restrains the formation of proper ferroelectric state, thus favouring the non-ergodic state. The partial substitution of Ba for Pb and Sn^{4+} for the B-type cations induces additional local structural deformations consisting mainly of BO_6 distortion along the three-fold and four-fold octahedral axes of symmetry, respectively.

1. Introduction

Relaxor ferroelectrics or relaxors are on the frontiers of modern solid-state science. They have been attracting considerable interest due to their outstanding dielectric, electro-optic, and electro-elastic properties, which are the basis of a number of technological applications including information storage and processing [1, 2]. Several peculiarities distinguish relaxors from proper ferroelectrics: (i) a diffuse phase transition over a temperature range, instead of an abrupt transition at the Curie point; (ii) a strong frequency dispersion of the dielectric permittivity as a function of temperature, and (iii) unusually small remnant polarization.

[4] Author to whom any correspondence should be addressed.

Besides, relaxors exhibit very weak or even no anisotropic response to long-coherent probe radiations like x-rays and polarized light, whereas conventional ferroelectrics have strong optical anisotropy and well-pronounced splitting of the Bragg reflections below the Curie point. In fact, on cooling, relaxors undergo several improper phase transitions: from paraelectric to ergodic (improper paraelectric) state, then to non-ergodic (improper ferroelectric) state and, finally, some relaxors go to long-range ferroelectric state. The ergodic state occurs at the so-called Burns temperature, well above the temperature of the dielectric-constant maximum, and is characterized by the existence of uncorrelated polar nanoclusters randomly distributed in a paraelectric matrix. The non-ergodic state occurs in the vicinity of the Curie range and may be preserved at lower temperatures. In the non-ergodic state the polar clusters interact on the intermediate-range scale only, without forming long-range ferroelectric domains.

The unique relaxor properties are related to the local structural distortions in the non-ergodic state. Due to the complexity and dynamical character of the nano-scale ferroic atomic clustering, studies of relaxors require the application of experimental techniques such as inelastic light and neutron scattering, transmission electron microscopy, nuclear magnetic resonance etc, in addition to the conventional diffraction methods [3–8]. Raman spectroscopy is beneficial in analysing the relaxor structure because of its sensitivity to length-scale (a few nanometres) and time-scale ($\sim 10^{-13}$–10^{-12} s). However, controversial interpretations of the observed Raman signals have been reported so far [9–12] and the origin of the phonon anomalies has still not been clarified. Lead-based perovskite-type compounds (ABO_3) are the major structural type of relaxor materials. To better understand the anomalous Raman scattering and its relation to the corresponding ferroic nanoclusters, we studied two representative relaxor compounds of perovskite type, $PbSc_{0.5}Ta_{0.5}O_3$ and $PbSc_{0.5}Nb_{0.5}O_3$, which have the same stoichiometric ratio and ionic radii of the B-site cations, i.e. the same tolerance factor $t = \frac{r_i(\mathrm{A})+r_i(\mathrm{O})}{\sqrt{2}(r_i(\mathrm{B})+r_i(\mathrm{O}))}$. The two materials differ from each other only in the B″-cation masses and B″–O atomic interactions, which allows for unambiguous recognition of the phonon modes generating the corresponding spectral peaks.

According to diffraction analyses, there are slight differences between the average structures of $PbSc_{0.5}Ta_{0.5}O_3$ and $PbSc_{0.5}Nb_{0.5}O_3$. Independently of the degree of compositional B-site ordering, $PbSc_{0.5}Nb_{0.5}O_3$ has rhombohedral $R3m$ symmetry in the ferroelectric state [13, 14]. The structural state of $PbSc_{0.5}Ta_{0.5}O_3$ seems to be more complicated. Originally, Setter and Cross [15] assumed a $Pm\bar{3}m$ cubic and a $R3m$ rhombohedral structure above and below the Curie temperature, respectively. Later it was shown that the paraelectric phase of partially and highly B-site ordered $PbSc_{0.5}Ta_{0.5}O_3$ is double-perovskite, with a face-centred cubic $Fm\bar{3}m$ symmetry, while the ferroelectric phase can be refined using the $R3m$ or $R3$ space-group symmetry [16–18]. Besides, electron diffraction studies revealed similarities between the crystal structures of $PbSc_{0.5}Ta_{0.5}O_3$ and $PbMg_{0.5}W_{0.5}O_3$, suggesting a weak or frustrated anfierroelectric state near the Curie range [19]. Actually, based on electron diffraction studies, additional ordering that involves anti-parallel displacements of Pb atoms was also assumed for highly B-site ordered $PbSc_{0.5}Nb_{0.5}O_3$ [20], which evidences that the local structures of $PbSc_{0.5}Ta_{0.5}O_3$ and $PbSc_{0.5}Nb_{0.5}O_3$ are very similar, but the correlation length of atomic displacements is longer for $PbSc_{0.5}Ta_{0.5}O_3$ (PST) compared to $PbSc_{0.5}Nb_{0.5}O_3$ [18]. Most probably the larger size of domains in PST is responsible for the additional subtle structural transformations at 233, 160, 100 and 50 K deduced from dielectric studies on PST films [21]. It was assumed that the electrical anomalies near 233 and 160 K are related to the lowering of the symmetry from rhombohedral to monoclinic and/or triclinic, whereas those near 100 and 50 K are related to further multiplication of the unit cell [21].

Herein we report on comparative analysis of the phonon anomalies and local structure in $PbSc_{0.5}Ta_{0.5}O_3$ and $PbSc_{0.5}Nb_{0.5}O_3$ single crystals and the effect of point defects (chemical variations in the cation positions) on the ferroic species in $PbSc_{0.5}Ta_{0.5}O_3$.

2. Experimental details

Cubic-shaped single crystals with a typical size of 1–3 mm and good optical quality were synthesized by the high-temperature solution growth method. The following compounds were analysed throughout this study:

- stoichiometric $PbSc_{0.5}Ta_{0.5}O_3$ (PST) and $PbSc_{0.5}Nb_{0.5}O_3$ (PSN);
- Nb-containing PST: (i) lightly doped, PST:Nb, with a ratio $Nb/(Sc + Ta) = 0.003$ and (ii) heavily doped, designated as PSTN, with a chemical formula $PbSc_{0.52}Ta_{0.35}Nb_{0.13}O_3$ or approximately 0.72PST–0.28PSN;
- Sn^{4+}-containing PST: (i) lightly doped, PST:Sn, with a ratio $Sn/(Sc + Ta) = 0.0001$ and (ii) heavily doped, designated as PSTS, with a chemical formula $PbSc_{0.40}Ta_{0.38}Sn_{0.22}O_3$ or approximately 0.78PST–0.22$PbSnO_3$;
- Ba-containing PST, designated as PBST, of chemical formula $Pb_{0.78}Ba_{0.22}Sc_{0.50}Ta_{0.50}O_3$.

The chemical composition was calculated from the content of metal elements determined by electron microprobe analysis (Cameca Microbeam SX100 SEM-system). The room-temperature crystal structure was probed by x-ray diffraction (XRD) analysis using a powder Philips X'Pert diffractometer and a single-crystal Nonius Kappa CCD diffractometer.

The Raman spectroscopic measurements were performed with a triple monochromator system Jobin-Yvon T64000 equipped with an Olympus BH2 microscope. The spectra were collected in back-scattering geometry using the 514.5 nm line of an Ar^+ laser with an output laser power of 1 W and focusing the incident light on the sample surface through a 50× long-distance objective. The spectral resolution was 2 cm^{-1}. Parallel and cross-polarized spectra were measured when the polarization of the incident light was parallel to the cubic edge and to the cubic face diagonal, i.e. using Porto notation, four scattering geometries were considered: $Z(XX)\bar{Z}$, $Z(XY)\bar{Z}$, $Z(X'X')\bar{Z}$ and $Z(X'Y')\bar{Z}$, where X, Y, Z, X' and Y' denote directions paralleling the [100], [010], [001], [110] and [$\bar{1}$10] crystallographic directions of a cubic class, respectively. The Raman scattering was recorded at different temperatures between 540 and 7 K using a Linkam heating/cooling stage and a Cryovac Konti–Cryostat-Mikro system for the experiments below 80 K. The measured Raman spectra were subsequently reduced by the Bose–Einstein phonon occupation factor to eliminate the temperature dependence of the peak intensities.

3. Results and discussion

The Raman scattering of PST and PSN measured at room temperature (291 K) in different experimental geometries is shown in figure 1. Several spectral features have to be considered:

(i) The same number of Raman peaks for both PST and PSN, which evidences the same symmetry of the fine-scale structure, in spite of the fact that the XRD analysis reveals a single-perovskite structure of $Pm\bar{3}m$ symmetry for PSN and a double-perovskite structure of $Fm\bar{3}m$ for PST (the atomic motif of the perovskite structure is shown in figure 2).

(ii) The intensification of some signals in the $Z(X'X')\bar{Z}$ geometry compared to the $Z(XX)\bar{Z}$ geometry and simultaneously their suppression in the $Z(X'Y')\bar{Z}$ compared to the $Z(XY)\bar{Z}$ geometry, which indicates that those signals are related to triply degenerate cubic modes.

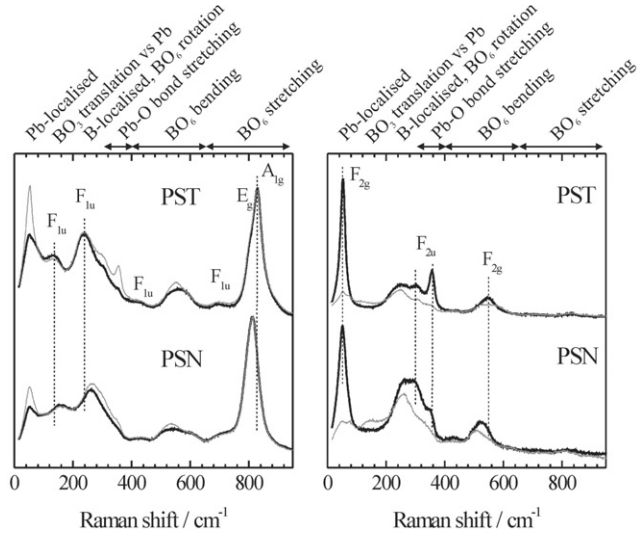

Figure 1. Room-temperature parallel (left-hand-side) and cross (right-hand-side) polarized spectra of PST and PSN. The bold black lines represent the spectra collected with the polarization of the incident light parallel to the cubic edge ($Z(XX)\bar{Z}$ and $Z(XY)\bar{Z}$), while the thin grey lines show the spectra collected with the polarization of the incident light parallel to the cubic face diagonal ($Z(X'X')\bar{Z}$ and $Z(X'Y')\bar{Z}$). The symmetry of the modes is given for the prototype $Fm\bar{3}m$ structure.

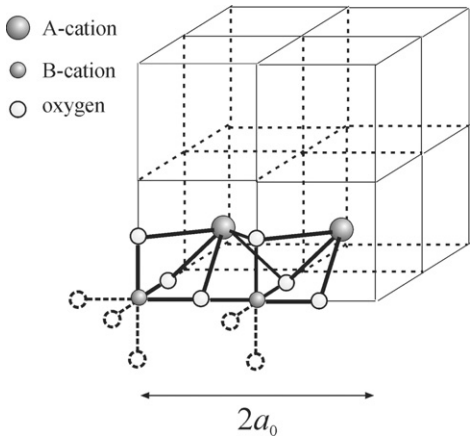

Figure 2. Atomic motif of a double-perovskite ABO_3 of $Fm\bar{3}m$ symmetry.

(iii) The higher positions of some peaks for PST compared to the PSN, which indicates that the peaks arise from O-localized octahedral modes, since the force constants between Ta and O are stronger than those between Nb and O [22].

(iv) The lower positions of some peaks for PST compared to PSN, which shows that the peaks arise from B-cation localized modes, since Ta is heavier than Nb.

The spectra can be best understood by considering the $Fm\bar{3}m$ symmetry of the prototype structure [23, 24]. According to group-theory analysis, there are $A_{1g}+E_g+F_{1g}+4F_{1u}+2F_{2g}+F_{2u}$ optical phonon modes at the Brillouin-zone centre. Four modes are Raman active: the BO_6 stretching modes of A_g and E_g symmetry, giving rise to the highest-wavenumber band near

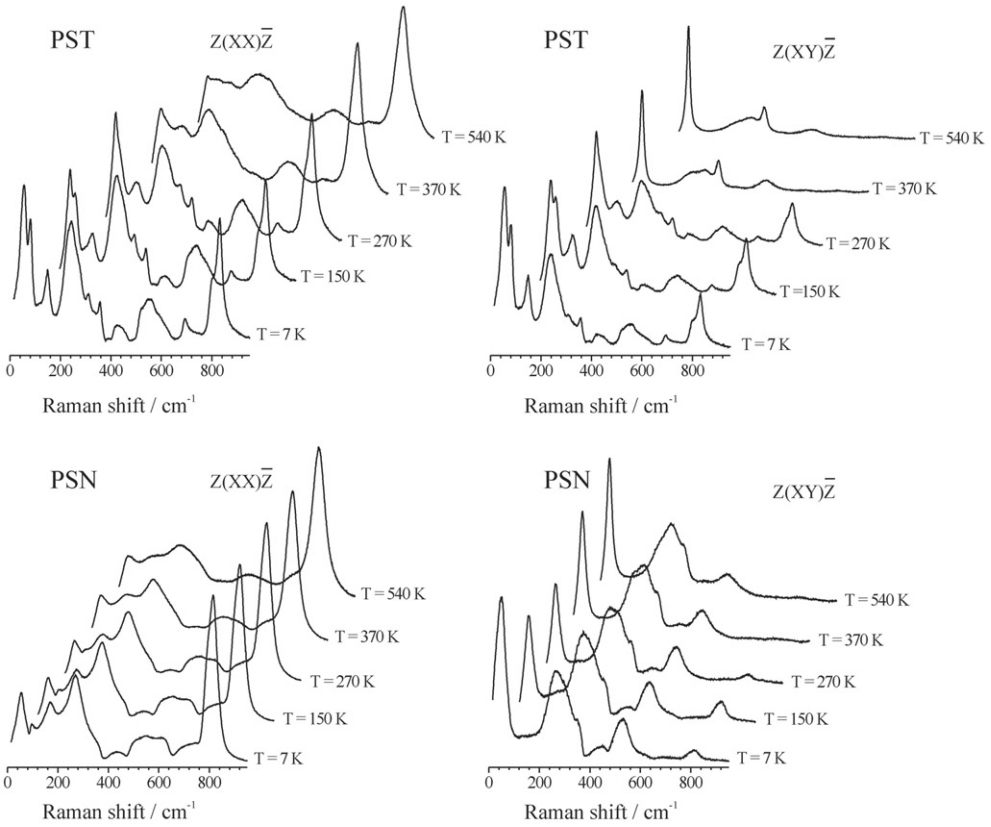

Figure 3. Polarized $Z(XX)\bar{Z}$ and $Z(XY)\bar{Z}$ spectra of PST and PSN measured at different temperatures in the range 540–7 K; the temperature of the paraelectric-to-ferroelectric phase transition is near to 280 and 360 K for PST and PSN, respectively.

820 cm^{-1} in the $Z(XX)\bar{Z}$ spectra, and the symmetrical BO_6 bending and Pb-localized modes of F_{2g} symmetry, generating the peaks near 540 and 50 cm^{-1}, respectively, in the $Z(XY)\bar{Z}$ spectra. All the other signals are 'dirty' modes and result from local structural deviations from the O_h symmetry of the average structure. The scattering near 250 cm^{-1}, which is stronger in the parallel polarized spectra, is mostly related to the B-cation localized F_{1u} mode. The O-localized BO_6 rotational mode F_{1g} should also contribute to the range 200–300 cm^{-1}. The bands near 700, 430 and 145 cm^{-1} are related to the anti-symmetrical BO_6 stretching, anti-symmetrical BO_6 bending and BO_6 translation F_{1u} modes, respectively. The scattering near 300–350 cm^{-1}, which is best pronounced in $Z(XY)\bar{Z}$, arises from Pb–O bond stretching vibrations and is related to the F_{2u} mode of the prototype structure. The Raman activity of the latter mode results from the non-coplanarity of Pb and O atoms in the {111} planes, and the intensity ratio $\rho = \frac{I(356)}{I(306)}$ is sensitive to the correlation length of coherent Pb shifts along the ⟨111⟩ directions [23, 24]. A larger value of ρ indicates a larger size of the quasi-two-dimensional (2D) spatial regions in which the Pb atoms are shifted in the same direction with respect to the plane of oxygen atoms, i.e. a larger size of the corresponding ferroic species. At room temperature, ρ for PST and PSN is equal to 0.67 ± 0.06 and 0.16 ± 0.01, respectively. Therefore, the main distinction between the ferroic clustering in PST and PSN is in the size of the quasi-2D spatial regions with coherent Pb shifts. The temperature dependence of the Raman scattering (figure 3) reveals that this structural difference leads to dissimilarity in the formation

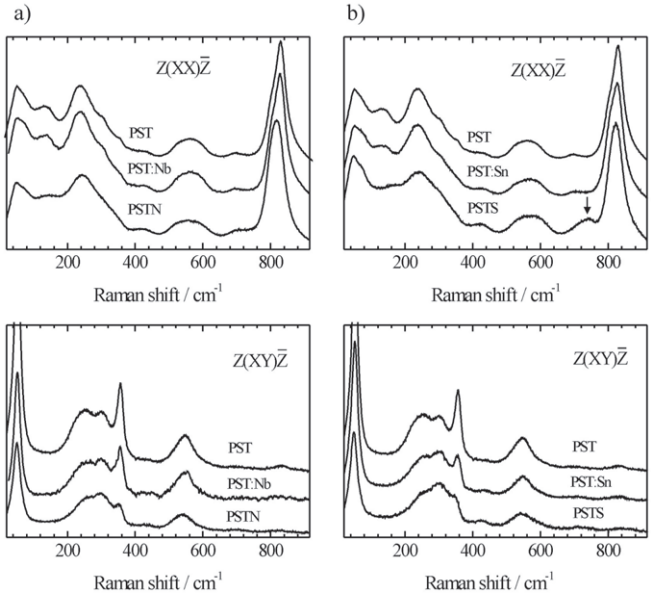

Figure 4. Room-temperature $Z(XX)\bar{Z}$ and $Z(XY)\bar{Z}$ spectra of (a) PST, Nb-doped PST with a Nb/Ta ratio = 0.006 (PST:Nb) and 0.72PST–0.28PSN (PSTN); and (b) PST, Sn-doped PST with a Sn/(Sc + Ta) ratio = 0.000 12 (PST:Sn) and 0.78PST–0.22$PbSnO_3$ (PSTS). The arrow points to the additional Raman scattering at 740 cm^{-1} induced by the incorporation of Sn.

of the ferroelectric state. The ferroelectric phase of PST and PSN is rhombohedral [14, 18] and thus the distortion of the unit cell is along the cubic body diagonal of the prototype structure. Therefore, the occurrence of the crystalline ferroelectric domains would result in the resemblance of the $Z(XX)\bar{Z}$ and $Z(XY)\bar{Z}$ spectra. The temperature of the dielectric-constant maximum for PST and PSN is near to 280 and 360 K [14, 25]. As can be seen in figure 3, the depolarization in the spectra of PST below 280 K is apparent, while for PSN no substantial spectral changes occur within the whole temperature range. Therefore, the ferroelectric state of PST consists of crystalline domains with established long-range ferroelectric ordering. The three-component splitting of the Raman scattering generated by the F_{2g} modes, which occurs below 180 K, reveals an additional phase transition from rhombohedral to monoclinic or triclinic symmetry [24]. Unlike PST, the ferroelectric state of PSN consists predominantly of a paraelectric isotropic substance with embedded polar nanoclusters. The gradual enhancement of the Raman scattering at 260 cm^{-1} in the $Z(XY)\bar{Z}$ geometry and thus the depolarization of this signal indicates the increase in spatial areas with the abundance of octahedral off-centre deviations of the B-site cations when the temperature is decreased.

To analyse the effect of the incorporation of an additional B-site cation on the ferroic clustering in PST, we have studied Nb- and Sn-doped PST. Figure 4 shows the spectra of Nb- and Sn-containing PST measured at 291 K. For both elements the doping leads to a gradual decrease in the intensity ratio ρ: 0.67–0.47–0.19 for the succession PST–PST:Nb–PSTN and 0.67–0.30–0.22 for the succession PST–PST:Sn–PSTS. Therefore, the inclusion of a third type of B-site cation also results in fragmentation of the incipient ferroic clusters associated coherent Pb shifts from the O atom planes perpendicular to the cubic body diagonal. In the case of Sn doping, an enhancement of the peak related to the anti-symmetrical BO_6 stretching F_{1u} mode is observed. This spectral feature indicates that the presence of Sn^{4+} cations in the B-position

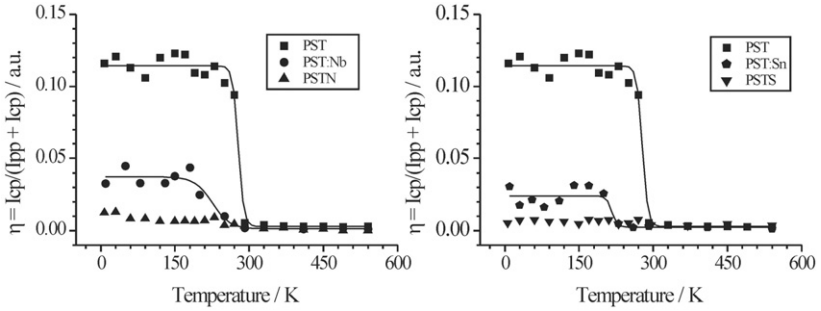

Figure 5. Temperature dependence of the ratio $\eta = \frac{I_{cp}}{I_{pp}+I_{cp}}$ for the series PST–PST:Nb–PSTN and PST–PST:Sn–PSTS. I_{cp} and I_{pp} denote the integrated intensity of the Raman-scattering band between 750 and 950 cm^{-1} measured in $Z(XY)\bar{Z}$ and $Z(XX)\bar{Z}$ geometries, respectively.

induces additional local structural deformation, namely octahedral distortion along one of the four-fold symmetrical axes of the BO_6 unit, thus varying the B–O bond lengths within the same octahedron. On cooling, the spectra of heavily doped PST samples preserve their polarization, while the lightly doped PST exhibit depolarization effects. The trend can be quantified by considering the temperature dependence of the intensity ratio $\eta = \frac{I_{cp}}{I_{pp}+I_{cp}}$, where I_{cp} and I_{pp} denote the integrated intensity of the Raman-scattering band between 750 and 950 cm^{-1} measured in the $Z(XY)\bar{Z}$ and $Z(XX)\bar{Z}$ geometries, respectively (figure 5). The ramp in the temperature dependence of η_{PST} occurs near 280 K, which corresponds to the paraelectric-to-ferroelectric phase transition temperature. For PST:Nb and PST:Sn the ramp is shifted to lower temperatures, and it is less than that for PST. Therefore, the size of long-range ferroelectric domains in the lightly B-site doped PST is substantially smaller than that in stoichiometric PST. It is worth noting that an additional lowering of rotational symmetry was not detected in either PST:Nb and PST:Sn. The low-temperature value of η for PST:Sn is smaller than that for PST:Nb, although the concentration of Sn is lower than that of Nb. This indicates that the embedding of Sn^{4+} restrains the long-range ferroelectric ordering in PST more strongly than Nb^{5+} does, which could be due to the occurrence of additional octahedral distortions. The ratio η for PSTN and PSTS remains close to zero for the whole temperature range, which shows that the heavy B-site doping impedes the development of crystalline ferroic domains.

In order to analyse the effect of A-site doping on the local structure and phonon anomalies, we have studied heavily Ba-doped PST. The Raman scattering of PBST measured at 291 K is shown in figure 6(a). As revealed by the smaller value of the intensity ratio ρ, the substitution of Ba for Pb also leads to a shorter correlation length of the coherent Pb displacements. The shift of the peaks arising from Pb–O bond stretching modes (denoted as I_2 and I_3 in figure 6) to higher wavenumbers indicates an enlargement of the AO_{12} polyhedron when the A-site is occupied by Ba and, consequently, a shortening of the adjacent Pb–O bonds (see figure 6(b)). The appearance of a well-pronounced peak at 441 cm^{-1} in the $Z(XX)\bar{Z}$ spectrum reveals additional variations in O–B–O bond angles of the BO_6 octahedra adjoining a Ba and a Pb cation, which is caused by the difference in the PbO_{12}- and BaO_{12}-polyhedral size (see figure 6(b)). All these spectral features evidence fragmentation of the intrinsic ferroic species and the generation of additional deformations, i.e. a wide distribution in size and shape of the incipient polar clusters, which explains the rather broad maximum of temperature dependence of the dielectric permittivity [26]. The dielectric experiments also show that the incorporation of Ba extends the non-ergodic state to lower temperatures, which is consistent with the preserved spectral polarization over the whole temperature range. One should mention that, in constrast to

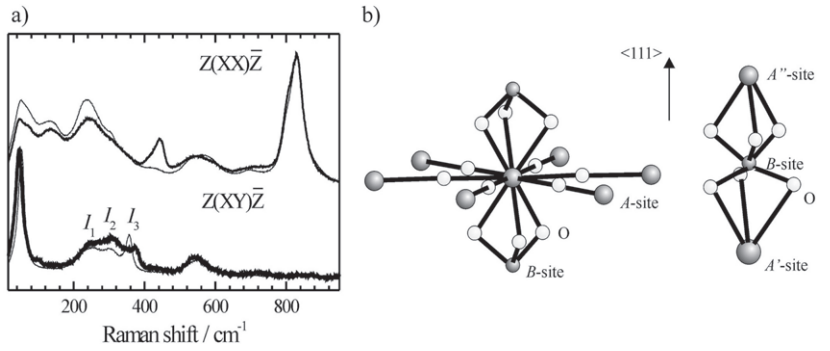

Figure 6. (a) Room-temperature $Z(XX)\bar{Z}$ and $Z(XY)\bar{Z}$ spectra of $Pb_{0.78}Ba_{0.22}Sc_{0.5}Ta_{0.5}O_3$ (bold lines) and PST (thin lines); the intensity ratio ρ for PBST is 0.14 versus 0.67 for PST. (b) The atomic surroundings of an A-site cation and a B-site cation adjoining two A-site cations with different ionic radii, $r_i(\mathrm{A}') > r_i(\mathrm{A}'')$.

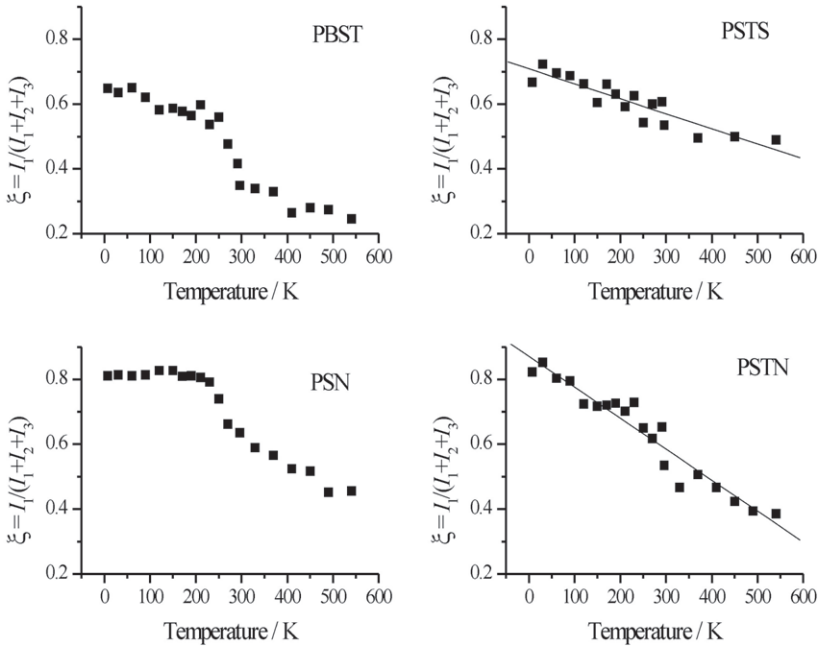

Figure 7. Temperature dependence of the ratio $\xi = \frac{I_1}{I_1+I_2+I_3}$ for samples which, on cooling, preserve their spectral polarization: $Pb_{0.78}Ba_{0.22}Sc_{0.5}Ta_{0.5}O_3$ (PBST), $PbSc_{0.5}Nb_{0.5}O_3$ (PSN), 0.78PST–0.22$PbSnO_3$ (PSTS) and 0.72PST–0.28PSN (PSTN). I_1, I_2 and I_3 denote the integrated intensities of the peaks near 250, 305 and 355 cm^{-1}, respectively, in $Z(XY)\bar{Z}$ geometry (see figure 6(a)).

the other heavily doped PST samples, PBST exhibits pronounced long-range compositional B-site ordering, with a degree of ordering of 0.23. However, as in the case of the PST samples poor and rich of oxygen vacancies, no apparent correlation between the degree of B-site ordering and the anomalous Raman scattering was observed.

The most resolved spectral change on a temperature decrease for the compounds that exhibit no or subtle depolarization of the spectra is the enhancement of the Raman scattering near 250 cm^{-1} in the $Z(XY)\bar{Z}$ geometry. Figure 7 shows the temperature dependence of the

ratio $\xi = \frac{I_1}{I_1+I_2+I_3}$ of PBST, PSN, PSTS and PSTN; I_1, I_2 and I_3 stand for the integrated intensities of the peaks near 250, 305 and 355 cm^{-1}, respectively (see figure 6(a)). Since the Raman scattering near 250 cm^{-1} is mostly related to the B-cation localized modes, the value of ξ is representative for the fraction of spatial regions with octahedral off-centre deviations of the B-cations. The change in ξ as a function of temperature reveals structural differences between PSN, A-site doped and heavily B-site doped PST. For PBST, a kink near 250 K is observed in the temperature dependence of the ratio ξ. This feature could be related to the additional octahedral deformation induced by the dilution of Pb with Ba and, hence, an enhancement of the intermediate-range interactions ferroic species based on such a local distortion. The heavily doped PST samples, PSTN and PSTS, exhibit a more or less linear temperature dependence of ξ, i.e. the fraction of ferroic clusters with B-cation off-centre shifts gradually increases when the temperature decreases. Interestingly, for PSN, the ratio ξ increases when the temperature decreases from 540 to 210 K and then remains nearly constant down to 7 K. This feature indicates a saturation of the corresponding local structural deformations at temperatures below 210 K.

4. Conclusions

The average size of the incipient quasi-two-dimensional ferroic species related to non-coplanarity of Pb and O atoms in layers perpendicular to the cubic body diagonal can be determined via the ratio $\rho = \frac{I(356)}{I(306)}$, where $I(356)$ and $I(306)$ are the integrated intensities of the corresponding peaks measured in the $Z(XY)\bar{Z}$ geometry at temperatures above and near the Curie range.

The development of long-range ferroelectric ordering can be followed by analysing the temperature dependence of the ratio $\eta = \frac{I_{cp}}{I_{pp}+I_{cp}}$, where I_{cp} and I_{pp} denote the integrated intensity of the Raman band near 850 cm^{-1} measured in $Z(XY)\bar{Z}$ and $Z(XX)\bar{Z}$ geometry, respectively.

For relaxors in which the main substance remains pseudo-cubic at temperatures well below the temperature of the dielectric-constant maximum, the fraction of spatial regions abundant of octahedral off-centre deviations of the B-cations can be estimated from the ratio $\xi = \frac{I_1}{I_1+I_2+I_3}$, where I_1, I_2 and I_3 are the integrated intensities of the peaks near 250, 305 and 355 cm^{-1} measured in the $Z(XY)\bar{Z}$ geometries.

$PbSc_{0.5}Ta_{0.5}O_3$ and $PbSc_{0.5}Nb_{0.5}O_3$ differ from each other in the length of coherence of Pb shifts from the O layers, which leads to dissimilarities in the ferroelectric state. The low-temperature phase of PST is composed of crystalline domains with established long-range ferroelectric ordering, whereas that of PSN consists of small-sized polar clusters distributed within an isotropic matrix. In PST, a nanoscale phase transformation involving lowering of the rotational symmetry occurs near 180 K. The incorporation of additional elements in the cation positions strongly influences the incipient ferroic clustering and restrains the formation of a proper ferroelectric state, thus favouring the non-ergodic state. The partial substitution of Ba for Pb and Sn^{4+} for the B-type cations induces additional local structural deformations consisting mainly of BO_6 distortion along the three-fold and four-fold octahedral axes of symmetry, respectively.

Acknowledgments

Financial support by the Deutsche Forschungsgemeinschaft (MI 1127/1-1) and the US National Science Foundation National Scientific Funds-Bulgarian Ministry of Education and Science (NT 1-02) is gratefully acknowledged.

References

[1] Bhalla A S, Guo R and Roy R 2000 *Mater. Res. Innov.* **4** 3
[2] Cordero F, Craciun F, Frabco A, Piazza D and Gallasi C 2004 *Phys. Rev. Lett.* **93** 097601
[3] Bursill L A, Julin P, Hua Q and Setter N 1995 *Physica* B **205** 305
[4] Husson E 1998 *Key Eng. Mater.* **155/156** 1
[5] Blinc R, Gregorovič A, Zalar B and Pirc R 2000 *Phys. Rev.* B **63** 024104
[6] Stock C, Ellis D, Swainson I P, Xu G, Hiraka H, Zhong Z, Luo H, Zhao X, Viehland D, Birgeneau R J and Shirane G 2006 *Phys. Rev.* B **73** 064107
[7] Haumont R, Gemeiner P, Dkhil B, Kiat J M and Bulou A 2006 *Phys. Rev.* B **73** 104106
[8] Bismayer U, Devarajan V and Groves P 1989 *J. Phys.: Condens. Matter* **1** 6977
[9] Siny I G, Katiyar R S and Bhalla A S 2000 *Ferroelectr. Rev.* **2** 51
[10] Jiang F, Kojima S, Zhao C and Feng C 2001 *Appl. Phys. Lett.* **79** 3938
[11] Kreisel J, Dkhil B, Bouvier P and Kiat J-M 2002 *Phys. Rev.* B **65** 172101
[12] Lina-Silva J J, Guedes I, Mendes Filho J, Ayala A P, Lente M H, Eiras J A and Garcia D 2004 *Solid State Commun.* **131** 111
[13] Perrin C, Menguy N, Suard E, Muller Ch, Caranoni C and Stepanov A 2000 *J. Phys.: Condens. Matter* **12** 7523
[14] Malibert C, Dkhil B, Kiat J M, Durand D, Bérar J F and Spasojevic-de Biré A 1997 *J. Phys.: Condens. Matter* **9** 7485
[15] Setter N and Cross L E 1980 *J. Mater. Sci.* **15** 2478
[16] Setter N and Cross L E 1980 *J. Appl. Phys.* **51** 4356
[17] Groves P 1985 *J. Phys. C: Solid State Phys.* **18** L1073
[18] Woodward P M and Baba-Kishi K Z 2002 *J. Appl. Crystallogr.* **35** 233
[19] Baba-Kishi K Z, Cressey G and Cernik R J 1992 *J. Appl. Crystallogr.* **25** 477
[20] Perrin C, Menguy N, Bidault O, Zahra C Y, Zahra A-M, Caranoni C, Hilczer B and Stepanov A 2001 *J. Phys.: Condens. Matter* **13** 10231
[21] Dawber M, Ríos S, Scott J F, Zhang Q and Whatmore R W 2001 *Fundamental Physics of Ferroelectrics 2001* (*AIP Conf. Proc. CP582*) ed H Krakauer (New York: American Institute of Physics) p 1
[22] Repelin Y, Husson E, Bennani F and Proust C 1999 *J. Phys. Chem. Solids* **60** 819
[23] Mihailova B, Bismayer U, Güttler B, Gospodinov M and Konstantinov L 2002 *J. Phys.: Condens. Matter* **14** 1091
[24] Mihailova B, Bismayer U, Güttler B, Gospodinov M, Boris A, Bernhard C and Aroyo M 2005 *Z. Kristallogr.* **220** 740
[25] Chu F, Setter N and Tagantsev A K 1993 *J. Appl. Phys.* **74** 5129
[26] Marinova V, Mihailova B, Malcherek T, Paulmann C, Lengyel K, Kovacs L, Veleva M, Gospodinov M, Güttler B, Stosch R and Bismayer U 2006 *J. Phys.: Condens. Matter* **18** L385